

**The Gauss-Legendre Sky Pixelization for the CMB polarization
(GLESP-pol). Errors due to pixelization of the CMB sky**

Andrei G. Doroshkevich

*Astro Space Center of Lebedev Physical Institute, Profsoyuznaya 84/32, Moscow, Russia,
dorr@asc.rssi.ru*

Oleg V. Verkhodanov

*Special Astrophysical Observatory, Nizhnij Arkhyz, Karachaj-Cherkesia, 369167, Russia,
vo@sao.ru*

Pavel D. Naselsky

Niels Bohr Institute, Blegdamsvej 17, DK-2100 Copenhagen, Denmark, naselsky@nbi.dk

Jaiseung Kim

Niels Bohr Institute, Blegdamsvej 17, DK-2100 Copenhagen, Denmark, jkim@nbi.dk

Dmitry I. Novikov

*Imperial College, London, United Kingdom,
Astro Space Center of Lebedev Physical Institute, Profsoyuznaya 84/32, Moscow, Russia,
d.novikov@imperial.ac.uk*

Viktor I. Turchaninov

Keldysh Institute of Applied Math, Russian Academy of Science, Moscow, 125047, Russia

Igor D. Novikov

*Astro Space Center of Lebedev Physical Institute, Profsoyuznaya 84/32, Moscow, Russia,
Niels Bohr Institute, Blegdamsvej 17, DK-2100 Copenhagen, Denmark,
Niels Bohr International Academy, Blegdamsvej 17, DK-2100 Copenhagen, Denmark,
novikov@asc.rssi.ru*

Lung-Yih Chiang

Institute of Astronomy and Astrophysics, Academia Sinica, P.O.Box 23-141, Taipei 10617,

Taiwan, Republic of China, lychiang@asiaa.sinica.edu.tw

Martin Hansen

Niels Bohr Institute, Blegdamsvej 17, DK-2100 Copenhagen, Denmark

We present developing of method of the numerical analysis of polarization in the Gauss–Legendre Sky Pixelization (GLESP) scheme for the CMB maps. This incorporation of the polarization transforms in the pixelization scheme GLESP completes the creation of our new method for the numerical analysis of CMB maps. The comparison of GLESP and HEALPix calculations is done.

1. Introduction

The analysis of the anisotropy of CMB temperature and polarization is one of the most effective methods for the extraction of the cosmological information and for tests of cosmology and fundamental physics.

The measurements of the anisotropy of CMB temperature performed by the WMAP mission allow us to establish parameters of the cosmological model of the Universe with unprecedented precision Refs. 1, 2, 3, 4.

Increasing sensitivity and angular resolution of the CMB data, including recently available WMAP 5 year data Ref. 2, ACBAR Ref. 5 QUaD Refs. 6,7, stimulates significant development and increasing predictability of the corresponding software (see, for instance, CAMB Ref. 8, COSMOMC Ref. 9, RICO Ref. 10, etc.)

During the next decade, after the PLANCK experiment, an investigation of the CMB polarization (including the B-mode) will be at the focus of the CMB science. Planning the CMBpol mission Ref. 11, B-pol mission Ref. 12, etc. requires significant improvement in estimation of the errors of the signal. Partially an uncertainties due to pixelization of the CMB sky and their propagation to the CMB power and the map can be potential sources of the error. For planning high resolution the CMB experiments the most frequently used the HEALPix package Ref. 13 as well as GLESP Ref. 14, ECP Ref. 15, and some others, needs to be tested in order to provide an exact information about the error bars of the convolution of the T , E , B -maps to the corresponding coefficients of the spherical harmonics decomposition not only for the power spectrum, but for the real and imaginary part of the coefficients as well.

The information about the multipole structure of the CMB signal is vital for the low multipoles ($\ell = 2, 3..$), since a lot of theoretical predictions about the properties of the cosmological model are related directly to the global morphology of the signal. As an example, we would like to mention widely discussed the Bianchi VII_h anisotropic cosmological model Refs. 16, 17, 18 which can mimic the anisotropy of the CMB power at the range of multipoles $\ell \leq 20$, and the Cold Spot Ref. 19 as well. The whole sky decomposition is vital for testing the alignment and planarity of the CMB anisotropy multipoles at $2 \leq \ell \leq 5$, discussed in Ref. 20 The exact information about the phases of the CMB signal is very useful for investigation of

statistical anisotropy and non-Gaussianity of the CMB Refs. 21, 22, 23, 24.

This Paper is devoted to presentation of a new package GLESP-pol (see Appendix), and investigation in details the errors of the standard transition “map to $a_{\ell,m}$ ” and vice versa for the most frequently used HEALPix 2.11 and newly released the GLESP-pol package. We would like to point out that both these packages reveal some peculiarities of the reconstruction of the coefficients of decomposition, especially for polarization. The major part of the error belongs to the $\ell, m = 0$, and $\ell, m = 2$ modes, when the simplest variants of decomposition were used. For the HEALPix 2.11, it is “zero iteration” key which blocks the correction of the $a_{\ell,m}$ taken from the map. For the GLESP-pol package, the maxima of the $a_{\ell,m}$ errors correspond to the GLESP 1.0 pixelization Refs. 14, 25. However, all these problems can be successfully resolved by implementation of iterations for the HEALPix 2.11 (the key “iterative analysis” 3 or 4 iterations) and the GLESP-pol pixelization for the polarization.

The outline of the paper is the follows. In Section 2, we discuss the difference between the HEALPix and the GLESP-pol scheme of the CMB sky pixelization, focusing on the polarization of the CMB. Section 3 is devoted to investigation of the errors of the “map $\rightarrow a_{\ell,m} \rightarrow$ map” transition for the CMB temperature anisotropy for the HEALPix and the GLESP-pol. In Section 4, we discuss the same issue for the Q,U Stokes parameters and E and B-modes of polarization. In Appendix the basic relations and description of the GLESP-pol package are presented.

2. Basic definitions

The temperature and polarization CMB anisotropy can be described in terms of the Stokes parameters T, Q, U through spherical harmonics decomposition $Y_{\ell,m}(\theta, \phi)$, and spin ± 2 spherical harmonics ${}_{\pm 2}Y_{\ell,m}(\theta, \phi)$

$$\begin{aligned} T(\theta, \phi) &= \sum_{\ell} \sum_{m} a_{\ell,m} Y_{\ell,m}(\theta, \phi), \\ Q(\theta, \phi) \pm iU(\theta, \phi) &= \sum_{\ell} \sum_{m} {}_{\pm 2}a_{\ell,m} {}_{\pm 2}Y_{\ell,m}(\theta, \phi) \end{aligned} \quad (1)$$

Here θ, ϕ are the polar and azimuthal angles of the polar system of coordinates, $a_{\ell,m}$ stands for the temperature anisotropy and the spin coefficients ${}_{\pm 2}a_{\ell,m}$ can be decomposed into E and B modes of polarization (see Appendix for details):

$${}_{\pm 2}a_{\ell,m} = -(a_{\ell,m}^E \pm ia_{\ell,m}^B), \quad a_{\ell,m}^{E,B} = (-1)^m (a_{\ell,-m}^{E,B})^* \quad (2)$$

The conversion of the T, Q, U signals to corresponding $a_{\ell,m}$ and ${}_{\pm 2}a_{\ell,m}$ coefficients is given by following integrals:

$${}_{0,\pm 2}a_{\ell,m} = \int_{-1}^1 dx \int_0^{2\pi} d\phi (T(x, \phi), Q(x, \phi), U(x, \phi)) {}_{0,\pm 2}Y_{\ell,m}^*(x, \phi), \quad (3)$$

where index 0 marks the temperature anisotropy, and $x = \cos \theta$. As it seen from Eq(3), the mathematical basis of any schemes of the pixelization of the CMB sky is very simple. We need to estimate the integrals in Eq(3) with very high accuracy taking into account the properties of discrete representation of the signal on the sphere. However, the modern CMB experiments normally deal with the incomplete sky due to peculiarities of design, scan strategy or implementation of different sort of mask. In this case the scheme of the pixelization of the sky become even more important, since we need to use the pixel domain for estimation of the power spectrum and investigation of the statistical properties of the CMB signal without implementation of the $_{0,\pm 2}a_{\ell,m}$ -coefficients. For these purpose the basic idea of the HEALPix package (equal area isolatitude pixelization) is very useful and more advanced in comparison to other pixelization. However, for the whole sky analysis of the T, Q, U signals $_{0,\pm 2}a_{\ell,m}$ -domain seems to be more optimal, in terms of the CPU timing, as from the scientific point of view. This is why in this paper we propose the GLESP-pol pixelization as complementary approach to the HEALPix package.

For numerical evaluation of the integral Eq(3), we use the Gaussian quadratures Ref. 14. This approach was proposed by Gauss in 1814, and developed later by Christoffel in 1877. As the integral over x in Eq. (3) is an integral over a polynomial of x we can use the following equality Ref. 26:

$$\int_{-1}^1 dx \Delta T(x, \phi) Y_{\ell m}^*(x, \phi) = \sum_{j=1}^N w_j \Delta T(x_j, \phi) Y_{\ell m}^*(x_j, \phi). \quad (4)$$

where both $\Delta T(x_j, \phi) Y_{\ell m}^*(x_j, \phi)$ and the proper Gaussian quadrature weighting functions, $w_j = w(x_j)$, are taken at points x_j which are the net of roots of the Legendre polynomial

$$P_N(x_j) = 0. \quad (5)$$

Here N is the maximal rank of the polynomial under consideration.

It is well known that the equation $P_N(x_j) = 0$ has N number of zeros in interval $-1 \leq x \leq 1$. For the Gaussian-Legendre method Eq(4), the weighting coefficients are

$$w_j = \frac{2}{1 - x_j^2} [P'_N(x_j)]^{-2}, \quad (6)$$

where $'$ denotes a derivative. They can be calculated together with the set of x_j with the 'gaulleg' code Ref. 26.

The old GLESP (version 1.0) pixelization scheme Ref. 25 was defined as follows:

- In the polar direction $x = \cos \theta$, we define $x_j, j = 1, 2, \dots, N$, as the net of roots of Eq. (5).
- Each root x_j determines the position of a ring with N_ϕ^j pixel centers with ϕ -coordinates ϕ_i .
- All the pixels have nearly equal area.
- Each pixel has weight w_j (see Eq (6)).

This scheme for the temperature anisotropy was realized in the publicly available code presented in `www.glesp.nbi.dk` and below we call it “GLESP 1.0” denoting as ‘grA’ (grid of equal areas). The new code GLESP-pol is based on the same definition of the roots of the Legendre polynomials, but different definition of the pixel area (see the item 3 from the top):

- All the rings have the same number of pixels (case ‘grN’ — grid of equal number of pixels in ring) by default. That is a cylindric projection of the sphere. We have also checked a special case when the number pixels of ring has an increment 4 starting from 10 pixels near the poles (case ‘grS’ — special grid). The old scheme (GLESP 1.0) when all the pixels have nearly equal area (grA) is also accessible.

In fig.1, we show the differences in pixelization of the GLESP 1.0, the GLESP-pol (grN), the GLESP-pol (grS) and the HEALPix. One can see, in the central part of the map the properties of the GLESP-pol (grN,grS) are the same as for the GLESP 1.0, but in the vicinity of the polar cups they are significantly different due to over-pixelization. This modification is vital for estimation of the $_{0,\pm 2}a_{\ell,m}$ -coefficients due to specific behaviour of $_{\pm 2}Y_{\ell,m}(\theta, \phi)$ -spherical harmonics (see Appendix for details).

3. Errors “ $a_{\ell,m} \rightarrow \text{map} \rightarrow a_{\ell,m}$ ” transition

This section is devoted to estimation of the error of the $a_{\ell,m}$ reconstruction by implementation different regimes of the HEALPix 2.11 and the GLESP-pol (grN and grS) packages. The error bars were defined in the following way. Let us take the coefficients $a_{\ell,m}^{T,E,B}$ for temperature anisotropy T and E and B modes of polarization for Λ CDM concordance model by implementation of the Monte Carlo simulation of the random Gaussian signal^a. For the C_{BB} -spectrum, we have taken a value equal to 10^{-11} just to escape zero in the test calculations.

Then, by implementation of the HEALPix 2.11 and the GLESP-pol packages we used these $a_{\ell,m}^{T,E,B}$ coefficients to create the map of the signal, keeping for both packages the same number of pixels. Thus, the HEALPix map M_H^i , and the GLESP-pol map M_G^p are defined as

$$M_H^i = \mathbf{H}a_{\ell,m}^{T,E,B}, \quad M_G^p = \mathbf{G}a_{\ell,m}^{T,E,B} \quad (7)$$

where \mathbf{H} and \mathbf{G} are the HEALPix and the GLESP-pol operators for “ $a_{\ell,m}$ to map” transition, the index i marks the number of iteration (0 as default, or 1-4), the index $p = 1$ marks the GLESP-pol grN pixelization, and $p = 2$ corresponds to the grS pixelization. Let us define the corresponding transition “map to $a_{\ell,m}$ ” as \mathbf{H}^{-1} for

^aWe have used the Gaussian signal for simplicity. However, only for the Gaussian signal the power spectrum $C(\ell) = (2\ell + 1)^{-1} \sum_{m=-\ell}^{\ell} |a_{\ell,m}^{T,E,B}|^2$ is the unique characteristic, which determines all the statistical properties.

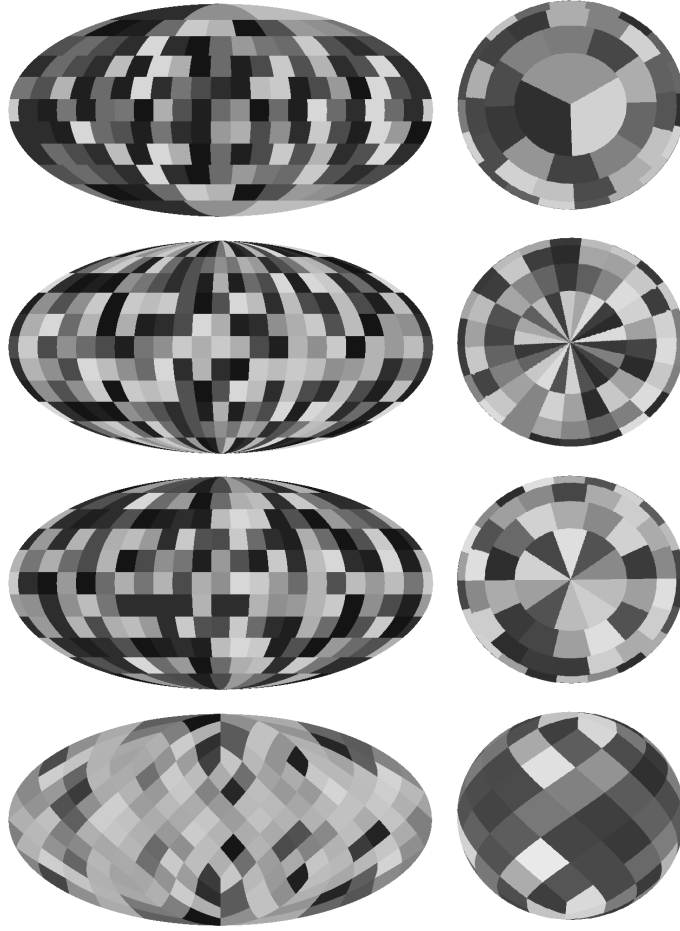


Fig. 1. Left column is the Mollweide projection of pixelization grids (from top to bottom): (a) the standard pixelization grid of the GLESP 1.0 (b) the GLESP-pol rectangular grid with the same number of pixels per each ring (the so called case ‘grN’), (c) the GLESP-pol grid with an pixel number increment 4 (case ‘grS’) starting from 10 pixels near poles but not greater than a given resolution in the equator ring, (d) the HEALPix grid. The right column shows the corresponding pixelization in the vicinity of the polar cups.

the HEALPix and \mathbf{G}^{-1} for the GLESP-pol:

$$\begin{aligned} b_{\ell,m}^{T,E,B} &= \mathbf{H}^{-1} M_H^i = \mathbf{H}^{-1} \mathbf{H} a_{\ell,m}^{T,E,B}, \\ c_{\ell,m}^{T,E,B} &= \mathbf{G}^{-1} M_G^p = \mathbf{G}^{-1} \mathbf{G} a_{\ell,m}^{T,E,B} \end{aligned} \quad (8)$$

where $b_{\ell,m}^{T,E,B}$ and $c_{\ell,m}^{T,E,B}$ are now the reconstructed coefficients for the HEALPix and GLESP-pol correspondingly. For idealistic case, when $a_{\ell,m} \rightarrow \text{map} \rightarrow a_{\ell,m}$ transition has no error bars, the reconstructed $b_{\ell,m}^{T,E,B}$ and $c_{\ell,m}^{T,E,B}$ have to be identical to the input coefficients $a_{\ell,m}^{T,E,B}$, and $\mathbf{H}^{-1} \mathbf{H} = \mathbf{H} \mathbf{H}^{-1} = \mathbf{I}$, $\mathbf{G}^{-1} \mathbf{G} = \mathbf{G} \mathbf{G}^{-1} = \mathbf{I}$,

where \mathbf{I} is just a unit matrix. In reality, neither the HEALPix, nor the GLESP-pol packages have non-zero error of the reconstruction due to window functions of the pixels and computational errors for the spherical harmonics. That means that corresponding absolute errors for the “ $a_{\ell,m} \rightarrow \text{map} \rightarrow a_{\ell,m}$ ” transition can be defined as follows:

$$\begin{aligned} R_{H\ell,m}^i &= \Re(b_{\ell,m}^{T,E,B}) - \Re(a_{\ell,m}^{T,E,B}), & I_{H\ell,m}^i &= \Im(b_{\ell,m}^{T,E,B}) - \Im(a_{\ell,m}^{T,E,B}), \\ R_{G\ell,m}^p &= \Re(c_{\ell,m}^{T,E,B}) - \Re(a_{\ell,m}^{T,E,B}), & I_{G\ell,m}^p &= \Im(c_{\ell,m}^{T,E,B}) - \Im(a_{\ell,m}^{T,E,B}), \end{aligned} \quad (9)$$

where \Re and \Im stand for the real and imaginary parts of the coefficients. Thus, the relative error is given by

$$\begin{aligned} r_{H\ell,m}^i &= \frac{R_{H\ell,m}^i}{\Re(a_{\ell,m}^{T,E,B})}, & y_{H\ell,m}^i &= \frac{I_{H\ell,m}^i}{\Im(a_{\ell,m}^{T,E,B})}, \\ r_{G\ell,m}^p &= \frac{R_{G\ell,m}^p}{\Re(a_{\ell,m}^{T,E,B})}, & y_{G\ell,m}^p &= \frac{I_{G\ell,m}^p}{\Im(a_{\ell,m}^{T,E,B})}, \end{aligned} \quad (10)$$

Note that defined in Eq(10) relative errors are related to the error of the power spectrum

$$\frac{\Delta C_\ell}{C_\ell} = \frac{\sum_m (|g_{\ell,m}|^2 - |a_{\ell,m}|^2)}{\sum_m |a_{\ell,m}|^2} = \frac{\sum_m |a_{\ell,m}|^2 (\delta_{\ell,m} + \delta_{\ell,m}^*)}{\sum_m |a_{\ell,m}|^2} \quad (11)$$

where $g_{\ell,m}$ and $a_{\ell,m}$ denote the reconstructed and input multipole coefficients, and $g_{\ell,m} = a_{\ell,m}(1 + \delta_{\ell,m})$. Taking into account that $\delta_{\ell,m} + \delta_{\ell,m}^* = 2\Re(\delta_{\ell,m})$ and $\Re(\delta_{\ell,m}) = [(\Re a_{\ell,m})^2 r_{\ell,m} + (\Im a_{\ell,m})^2 y_{\ell,m}] / |a_{\ell,m}|^2$, where $r_{\ell,m}$ and $y_{\ell,m}$ denote relative errors for real and imaginary parts from Eq(10), we gets:

$$\frac{\Delta C_\ell}{C_\ell} = 2 \frac{\sum_m [(\Re a_{\ell,m})^2 r_{\ell,m} + (\Im a_{\ell,m})^2 y_{\ell,m}]}{\sum_m |a_{\ell,m}|^2} \quad (12)$$

From Eq(12) clearly seen that the error of reconstruction of real and imaginary part of each ℓ, m coefficient propagates to the error of the power spectrum through weighting coefficients

$$w_{\ell,m}^r = \frac{(\Re a_{\ell,m})^2}{\sum_m |a_{\ell,m}|^2}, \quad w_{\ell,m}^y = \frac{(\Im a_{\ell,m})^2}{\sum_m |a_{\ell,m}|^2} \quad (13)$$

and formally depends on the power spectrum and the morphology of the input signal. This is why in addition to the input random Gaussian CMB signal we will discuss the errors of reconstruction of the multipoles and the power spectrum for very asymmetric maps, like WMAP 5 Q and V bands.

3.1. Errors for HEALPix and GLESP-pol temperature anisotropy

We will start our analysis from estimation of the dynamical range of variations of the temperature anisotropy for $N_{\text{side}}=1024$. For that we will use the input signal, which corresponds to random Gaussian CMB, and Internal Linear Combination Map (WILC5) from the LAMBDA archive (<http://lambda.gsfc.nasa.gov/>) and corresponding K, Ka, Q, V and W total channels maps. In Fig2 we plot the diagram $A(i)$ versus $A(th)$, where $A(i) = \text{string}(|a_{\ell,m}|)$, where the operator "string" transforms the $|a_{\ell,m}|$ coefficients to one dimensional string $|a_{1,0}|, |a_{1,1}| \dots$ for K–W bands, and $A(th)$ is the string for the random Gaussian CMB signal. From this diagram

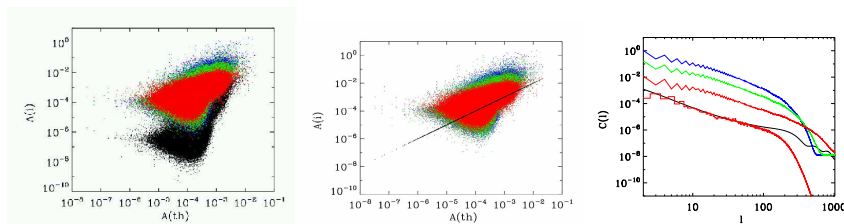


Fig. 2. Left. The $A(i)$ versus $A(th)$ diagram for the WILC5 (the black dots), K-band (the blue dots), KA-band (the green dots), V-band (the red dots). Both $A(i)$ and $A(th)$ are in mK. Middle. The same as the left plot, but for replacement of the WILC5 by $A(th)$. Right. The power spectrum $C(\ell)mK^2$ for the WILC5 (the red bottom line), for random realization (the black line), the K band (the solid blue line), the KA-band (the green solid line), and for V band (the red solid line).

one can see that, for example, to estimate the $a_{\ell,m}$ coefficients by using ILC method we should have, at least, the relative error better than $10^{-3} - 10^{-4}$ if the low frequency K-band is included to the analysis. The accuracy of the $a_{\ell,m}$ coefficients should be about 3–4 orders of magnitude better if we are interested in different sort of coupling between different multipoles (so called the non-Gaussianity tool).

To estimate the errors of the $a_{\ell,m} \rightarrow \text{map} \rightarrow a_{\ell,m}$ transition, let us start from the analysis of the temperature anisotropy for the HEALPix 2.11 and the GLESP-pol packages. In Fig.3, we show the maps for $b_{\ell,m}^0 - a_{\ell,m}$ -signal, where $b_{\ell,m}^0$ obtained by implementation of the HEALPix 2.11 "zero iteration" key (top left map) and 4 iterations (top right map).

One can see, that the top left map reveals all the peculiarities of the pixelization, localized at the vicinity of the North and the South poles. The top left plot show the map of differences, but after 4 iterations. No visible large scale defects can be found. The bottom left and right maps represent the GLESP-pol pixelization without any iterations for the same number of pixels, as the top one. In Fig.4, we plot the real and imaginary parts of the absolute errors from Eq(9) for the maps, shown in fig.3).

The definition of function $A(in)$ and r in Fig.4 is the following: $A(in) = \text{string}(a_{\ell,m})$, where the operator "string" transforms the $a_{\ell,m}$ coefficients to one dimensional string $a_{1,0}, a_{1,1}, \dots$, and $r = |r_{H\ell,m}^0, r_{H\ell,m}^4, y_{H\ell,m}^0, y_{H\ell,m}^4|$ (see Eq.(10).

Fig.4 clearly show that the HEALPix 2.11 (no iteration) reconstruction is differ-

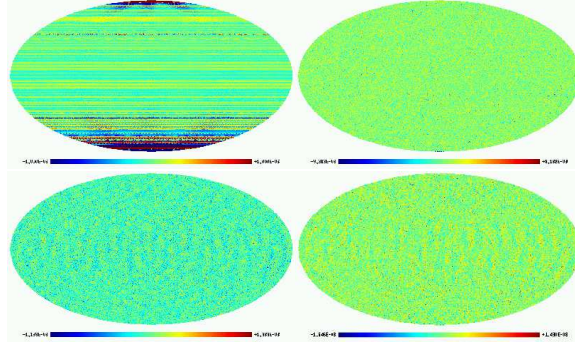


Fig. 3. The differences of reconstructed and input maps for the HEALPix2.11 (the top pair) and the GLESP-pol (the bottom pair). Top left plot corresponds to “zero iteration“ key (the color scale is $-10^{-6}, 10^{-6}mK$), top right is for 4 iterations (the color scale is $-10^{-8}, 10^{-8}mK$). Bottom left—the GLESP-pol reconstruction for the grN mode (the color scale is $-10^{-8}, 10^{-8}mK$). Top right corresponds to the grS mode (the color scale is $-10^{-8}, 10^{-8}mK$). The number of pixels for the HEALPix2.11 and the GLESP-pol are practically the same. No correction by the window function of the pixels.

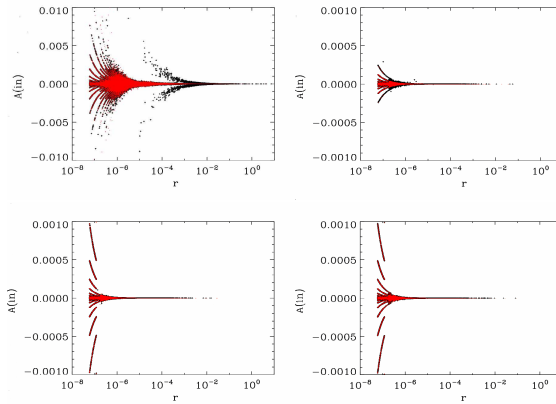


Fig. 4. The errors of reconstructions for the HEALPix2.11 (the top pair) and the GLESP-pol (the bottom pair). Top left plot corresponds to “zero iteration” key, top right is for 4 iterations. Bottom left — the GLESP-pol reconstruction for the grN mode. Top right corresponds to the grS mode. Black dots corresponds to the real part of ℓ, m modes, the red dots show for the imaginary part.

ent for the real and imaginary parts of the signal. For real part (see Fig.4, top left), the relative error has the secondary zone, localized at $r > 10^{-5}$, while for imaginary part the major part of the points belongs to $r < 10^{-5}$. Note that even after implementation of 4 iterations for the HEALPix2.11 and grN, grS modes of the GLESP-pol, there exists a very small number (~ 10) of modes with error 1%-10%. Thus, the main conclusion is that for $N_{\text{side}}=1024$ the HEALPix iterations significantly improve the global morphology of the map and the error of reconstruction,

which is practically the same the HEALPix and the GLESP-pol.

The next question, which we would like to discuss, is how the error of reconstruction depends on the number of pixels and their size. Both these parameters are determined by the choice of N_{side} for the HEALPix, or by the maximal resolution of the map ℓ_{max} for the GLESP-pol. Answering this question in Fig.5 and Fig.6, we plot the corresponding maps of errors and $A(in)$ versus r diagrams, similar to Fig.3 and Fig.4, but for less number of pixels.

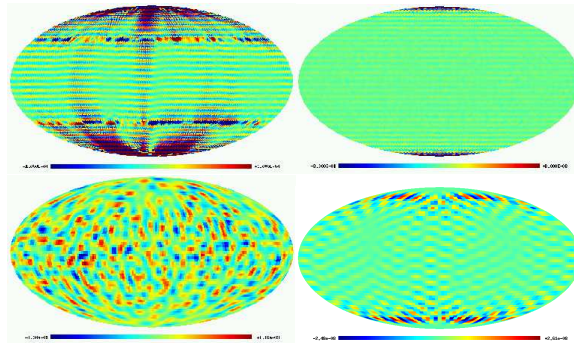


Fig. 5. The differences of reconstructed and input maps for the HEALPix 2.11 for $N_{\text{side}}=32$ (the top pair) and the GLESP-pol (the bottom pair). Top left plot corresponds to “zero iteration” key (the color scale is $-10^{-4}, 10^{-4} mK$), top right is for 4 iterations (the color scale is $-8 \cdot 10^{-8}, 8 \cdot 10^{-8} mK$). Bottom left — the GLESP-pol reconstruction for the grN mode (the color scale is $-10^{-8}, 10^{-8} mK$). Bottom right corresponds to the grS mode (the color scale is $-2.5 \cdot 10^{-8}, 2.5 \cdot 10^{-8} mK$). The number of pixels for the HEALPix 2.11 and the GLESP-pol are practically the same. No correction by the window function of the pixels.

It would be important to note that as for the high resolution map of difference, shown in Fig.3, as for the low resolution map (see Fig.5) for the HEALPix 2.11 with zero iteration the major component of the error is related to $b_{\ell, m=0}$ mode. These harmonics manifest themselves as horizontal lines parallel to the Galactic plane. Two horizontal lines with high amplitude signal along mark the HEALPix zones, where the number of pixels for each equal latitude ring start to decrease, when $\theta \rightarrow 0$ (the North pole), or $\theta \rightarrow \pi$ (the South pole). However, after 4 iterations all these peculiarities of the map of errors were significantly suppressed, except two zones around the North and the South cups. For the GLESP-pol package with $\ell_{\text{max}} = 32$ the minimal level of errors for the reconstructed map is given by the grN pixelization, when $r \ll 10^{-7}$ for major part of the pixels, and $r \ll 10^{-5}$ for the grS pixelization. It would be important to note that the accuracy of reconstruction of real and imaginary parts of the coefficients of expansion are different for the HEALPix and the GLESP-pol. As it is follows from Fig4 and Fig6, the HEALPix recovers the imaginary part significantly better than a real one even for zero iteration mode. The GLESP-pol reconstructs real and imaginary parts with nearly equal errors.

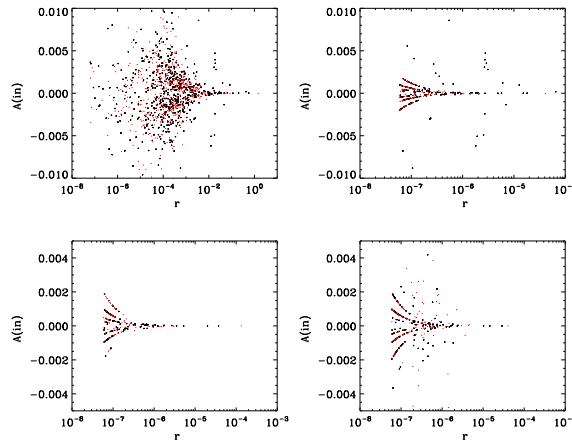


Fig. 6. The errors of reconstructions for the HEALPix 2.11 (Nside=32) (the top pair) and the GLESP-pol (the bottom pair). Top left plot corresponds to “zero iteration” key, top right is for 4 iterations. Bottom left — the GLESP-pol reconstruction for the grN mode. Top right corresponds to the grS mode. Black dots corresponds to the real part of ℓ, m modes, the red dots are for imaginary part.

4. The GLESP-pol and the HEALPix polarization.

As we have mentioned already in Introduction, the GLESP-pol pixelization was designed to assess the problem of accurate reconstruction of the coefficients of spin ± 2 spherical harmonics decomposition (see Appendix for details). Since the spin ± 2 spherical harmonics have a peculiarity, from the computational point of view, behaviour in the vicinity of the polar cups, the differences in the GLESP-pol polarization and the HEALPix produce different error of reconstruction and become more visible especially for polarization. In Fig.7, we plot the map of differences between input and output signal, reconstructed by the GLESP-pol (grN and grS pixelization).

As one can see from this figure, the reconstruction of Q and U components by the grN and grS pixelization is characterized by very high accuracy, but the grN pixelization looks slightly better. For the HEALPix 2.11 the corresponding maps for differences are shown in Fig.8.

For low resolution pixelization with Nside=32 and $\ell_{max} = 32$ the corresponding maps are shown in Fig.9

Thus, one can see that implementation of the 4 iterations for the HEALPix package gives us practically the same result, as from GLESP-pol even for the low resolution maps (see Fig.10). In Fig.11 we show the diagram, similar to the Fig.4, but for E and B components of polarization.

One can see that the GLESP-pol mode grN gives us practically the same errors, as the HEALPix 2.11 4 iteration mode. However, the CPU time for the GLESP-pol is about 4 time smaller then for the HEALPix 2.11 due to absence of iterations.

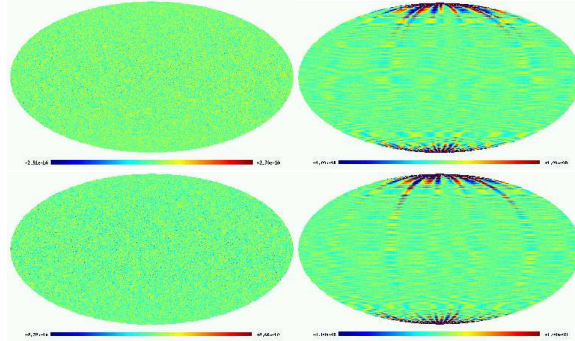


Fig. 7. The differences of reconstructed and input maps for the GLESP-pol for $\ell_{max} = 1500$ (the top pair is for Q the Stokes parameter) and the bottom pair is for U). Top left plot corresponds to the grN pixelization (the color scale is $-3 \cdot 10^{-10}, 3 \cdot 10^{-10} mK$), top right is for the grS pixelization (the color scale is $-10^{-9}, 10^{-9} mK$). Bottom left — the GLESP-pol reconstruction of Q for grN mode (the color scale is $-2.5 \cdot 10^{-10}, 2.5 \cdot 10^{-10} mK$). Bottom right corresponds to the grS mode (the color scale is $-10^{-9}, 10^{-9} mK$).

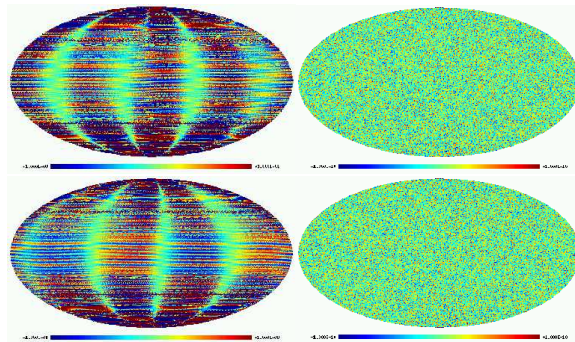


Fig. 8. The differences of reconstructed and input maps for the HEALPix 2.11 for $N_{side}=1024$ (the top pair corresponds to Q components and the bottom pair is for U). Top left plot corresponds to the “zero iteration” key (the color scale is $-10^{-8}, 10^{-8} mK$), top right is for 4 iterations (the color scale is $10^{-10}, 10^{-10} mK$). Bottom left — the GLESP-pol reconstruction for the grN mode (the color scale is $10^{-8}, 10^{-8} mK$). Bottom right corresponds to the grS mode (the color scale is $-10^{-10}, 10^{-10} mK$). The number of pixels for the HEALPix 2.11 and the GLESP-pol are practically the same. No correction by the window function of the pixels.

Finally, we demonstrate absolute relative accuracy for power spectra ($\Delta C(\ell)/C(\ell)$) for the GLESP 2.0 (grS and grN) and for the HEALPix 2.11 (0 and 4 iteration modes) shown in Fig. (12). As one could see the relative accuracy for restoration of the power spectrum of temperature anisotropy in the GLESP is approximately the same for both types grS and grN, and the HEALPix 4 iteration mode give better accuracy at low multipoles and reaches the GLESP one at higher. For polarization, we have approximately the same accuracy for the GLESP grN and HEALPix 4 iteration modes.

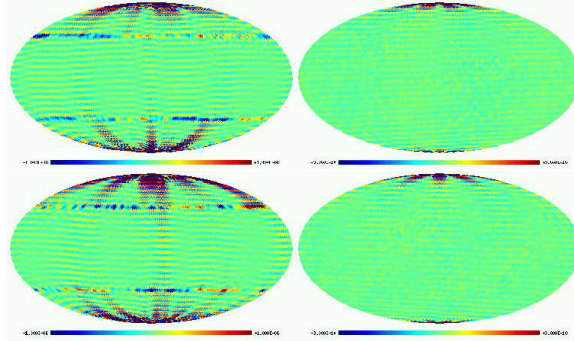


Fig. 9. The differences of reconstructed and input maps for the HEALPix 2.11 for $N_{\text{side}}=32$ (the top pair corresponds to Q components and the bottom pair is for U. Top left plot corresponds to the “zero iteration” key (the color scale is $-10^{-6}, 10^{-6} mK$), top right is for 4 iterations (the color scale is $-3 \cdot 10^{-10}, 3 \cdot 10^{-10} mK$). Bottom left — the U component for the zero iteration (the color scale is $-10^{-6}, 10^{-6} mK$). Bottom right corresponds to 4 iterations (the color scale is $-3 \cdot 10^{-10}, 3 \cdot 10^{-10} mK$).

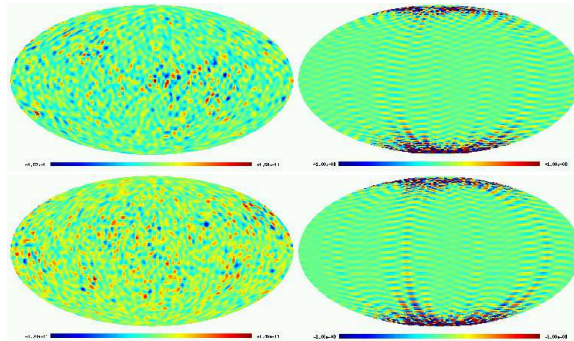


Fig. 10. The errors of reconstructions for the GLESP-pol (Q for the top pair and U for the bottom pair). Top left plot corresponds to the grN pixelization (the color scale is $-2 \cdot 10^{-11}, 2 \cdot 10^{-11} mK$), top right is for grN (the color scale is $-10^{-8}, 10^{-8} mK$). Bottom left — the GLESP-pol reconstruction for the grS mode (the color scale is $-2 \cdot 10^{-11}, 2 \cdot 10^{-11} mK$). Bottom right corresponds to the grS mode (the color scale is $-10^{-8}, 10^{-8} mK$).

5. Conclusions

Here we present the GLESP-pol package which incorporates calculations of polarization on the sphere into the CMB analysis package based on the Gauss–Legendre Sky Pixelization. We developed corresponding software for data processing.

According to our numerical calculations, the described scheme for polarization preserves the same level of precision as GLESP 1.0 can provide for the temperature anisotropy.

The code continues to be developed now and different definitions of polarization modes Refs. 27, 13 are planned to be included. GLESP-pol is open for new approaches and could be implemented for extension of the present code, e.g. such as

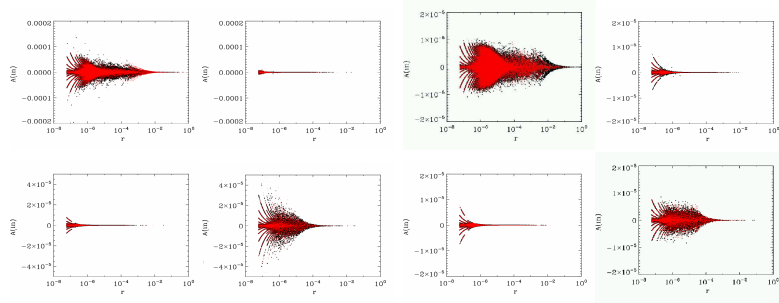


Fig. 11. The errors of reconstructions of $\text{Re}a_{\ell,m}^E$ and $\text{Im}a_{\ell,m}^E$. Top row corresponds to the HEALPix 2.11 ($N_{\text{side}}=1024$). From the left to the right are: E mode with zero iteration, E mode with 4 iteration, B mode with zero iteration, B mode with 4 iteration. Bottom row is the same, but for the GLESP-pol grN and grS modes and $\ell_{\text{max}} = 1500$. Black dots corresponds to the real part of ℓ, m modes, the red dots are for imaginary part.

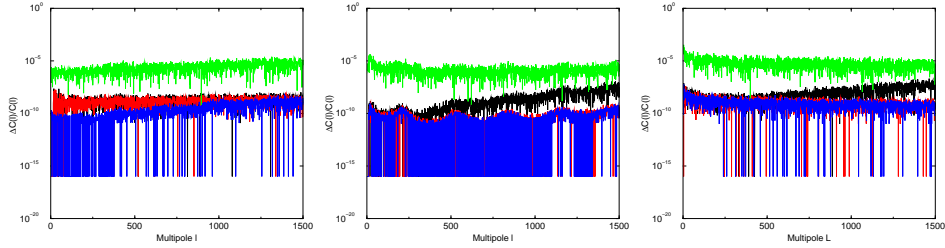


Fig. 12. The relative accuracy of $C(\ell)$ spectrum restoration for temperature anisotropy (left), E-polarization (middle) and B-polarization (right). The grS GLESP type is shown with the black line, the grN type is shown with red, the HEALpix calculations of $C(\ell)$ of 0 iteration mode are plotted with green color, and of 4 iteration with blue.

the fast spin-weighted harmonics calculation Ref. 28. A completely new algorithm for fast Spherical Harmonics Transform has been proposed recently by Mark Tygert Ref. 29. It is worth mentioning that this algorithm can be applied only for GLESP pixelization of the sky and effective as $O(A \times \ell^2 \text{Log}_2 \ell)$ operations instead of usual $O(\ell^3)$. Unfortunately a huge prefactor A makes this algorithm only about 3 times faster than existing HEALPix and GLESP for $\ell = 2048$.

The most important part of our investigation is that the HEALPix 2.11 package provides the same accuracy as the GLESP-pol only by implementation of 4 iterations. The zero iteration mode of the HEALPix 2.11 can provide significant error for the coefficients of expansion and be used with caution.

Acknowledgments

Athours are very thankful to Radek Stompor for useful remarks to the paper and to Per Rex Christensen for very fruitful discussions and checking GLESP procedures. This paper was supported in part by the RFBR grants 07-02-00886, 08-02-00090,

08-02-00159, 09-02-00298, by S.S. 2469.2008.2 and by FNU grants 272-06-0417, 272-07-0528 and 21-04-0355.

References

1. Hinshaw, G. et al., *ApJS***170**, 288 (2007)
2. Hinshaw, G. et al., *ApJS***180**, 225 (2009)
3. Spergel, G. et al., *ApJS***170**, 377 (2007)
4. Nolta, M.R. et al., *ApJS***180**, 296 (2009)
5. Reichardt, C. L. et al., arXiv:0801.1491 (2008)
6. Pryke, C. et al., *ApJ***692**, 1247 (2009)
7. Hinderks, J. R. et al., *ApJ***692**, 1247 (2009)
8. Challinor A., Lewis A. *Phys.Rev. D* **71**, 103010 (2005)
9. Lewis A., Bridle S. *Phys.Rev.D* **66**, 103511, (2002)
10. Fendt, W. A., Chluba, J., Rubino-Martin, J. A., Wandelt, B. D. arXiv:0807.2577 (2008)
11. Baumann, D. et al., arXiv:0811.3919 (2008)
12. de Bernardis P. et al., arXiv:0808.1881 (2008)
13. Górski, K.M., Hivon, E., Banday, A. J., et al., *ApJ***622**, 759 (2005)
14. Doroshkevich A.G., Naselsky P.D., Verkhodanov O.V., et al. *Internat. J. Modern Physics D* **14**, 275 (2005), astro-ph/0305537
15. Muciaccia P. F., Natoli P. and Vittorio N., *Astrophys.J.* **488**, 63 (1997)
16. Eriksen, H. K. et al., *ApJ* 605, **14** (2004) astro-ph/0307507
17. Jaffe, T. et al., *ApJ* **629**, L1 (2005), astro-ph/0503213
18. Bridges, M., McEwen, J. D., Lasenby, A. N., Hobson, M. P. *MNRAS***377**, 1473 (2007)
19. Cruz M., Martinez-Gonzales E., Vielva P., Cayon L., *MNRAS*, 356, 29, 2005, astro-ph/0405341
20. Eriksen, H. K. et al., *ApJ* 612, 633 (2004), astro-ph/0403098
21. Chiang Lung-Yih, Naselsky P.D., Verkhodanov O.V., Way M.J. *ApJ***590**, L65 (2003), astro-ph/0303643
22. Naselsky P.D., Doroshkevich A.G., Verkhodanov O.V. *ApJ***599**, L53 (2003), astro-ph/0310542
23. Naselsky P.D., Doroshkevich A.G., Verkhodanov O.V. *MNRAS***349**, 695 (2004), astro-ph/0310601
24. Naselsky P.D., Novikov D.I., Novikov I.D., *The Physics of the Cosmological Microwave Background*, Cambridge University Press (2006)
25. Doroshkevich A.G., Naselsky P.D., Verkhodanov O.V., et al., astro-ph/0501494, (2005)
26. Press, W.H., Teukolsky, S.A., Vetterling, W.T., & Flannery, B.P., *Numerical Recipes in FORTRAN*, Second Edition, Cambridge University Press (1992)
27. Kamionkowski, M., Kosowsky, A., Stebbins, A., *Ph.Rev. D* **55**, 7368 (1997)
28. Wiaux, Y., Jacques, L., Vanderghynst, P., *ApJ***632**, 15 (2005), astro-ph/0502486
29. Tytgert M., *J. Comput. Phys.* **227**, 4260 (2008)
30. Varshalovich, D.A., Moscalev, A.N., Khersonskii, V.K., 'Quantum Theory of Angular Momentum', (Singapore: World Scientific, 1989)
31. Lewis, A., Challinor, A., Turok, N., *Phys. Rev. D* **65b**, 3505 (2002), astro-ph/0106536
32. Zaldarriaga, M. & Harari, D., *Phys. Rev. D* 52 3276 (1995)
33. Zaldarriaga, M. & Seljak, U., *Phys. Rev. D* 55 1830 (1997)
34. Seljak, U. & Zaldarriaga, M., *Phys. Rev. Lett.* 78, 2054 (1997).
35. Frigo, M. & Johnson, S.G., 1997, *The Fastest Fourier Transform in the West*, Technical Report MIT-LCS-TR-728, 1997, <http://www.fftw.org>

36. Hanisch R.J., Farris A., Greisen E.W., et al. *Astron. Astrophys.*, **376**, 359 (2001)

6. Appendix

6.1. Description of polarization

6.1.1. Basic relations for the flat space

The polarization is characterized by the symmetric traceless matrix \mathbf{T} composed by two Stokes parameters, $Q(\mathbf{x})$ & $U(\mathbf{x})$:

$$\mathbf{T} = \begin{pmatrix} Q & U \\ U & -Q \end{pmatrix} \quad (14)$$

The functions Q and U depend upon the coordinate frame and components of the tensor T_i^j obey the corresponding tensor transformation law:

$$\tilde{T}_i^j = O_i^k O_\ell^j T_k^\ell \quad (15)$$

where the coordinate transformation is given by $\tilde{x}^i = O_k^i x^k$. In particular case under rotation of the coordinate system with the rotation angle ϕ

$$\mathbf{O} = \begin{pmatrix} \cos \phi & \sin \phi \\ -\sin \phi & \cos \phi \end{pmatrix} \quad (16)$$

the functions Q and U are transformed as:

$$\begin{aligned} Q' &= Q \cos 2\phi + U \sin 2\phi \\ U' &= -Q \sin 2\phi + U \cos 2\phi \end{aligned} \quad (17)$$

The intensity $I^2 = Q^2 + U^2 = \frac{1}{2} T_i^k T_k^i$ does not depend upon the coordinate system.

6.1.2. Basic relations on the sphere

An arbitrary traceless symmetric tensor can be presented in terms of scalar “electrical”, E , and pseudo-scalar “magnetic”, B , potentials as:

$$T_{ij} = \left(E_{;i;j} - \frac{1}{2} g_{ij} E_{;k}^k \right) + \frac{1}{2} \left(\epsilon_{ik} B_{;j}^k + \epsilon_{jk} B_{;i}^k \right). \quad (18)$$

where ϵ_{ij} is the completely antisymmetric tensor ($\epsilon_{11} = \epsilon_{22} = 0$, $\epsilon_{12} = -\epsilon_{21} = -\sin\theta$) and ‘;’ denotes covariant differentiation on the two dimensional sphere with the metric

$$dl^2 = d\theta^2 + \sin^2 \theta d\varphi^2$$

Here θ, φ are the polar and azimuthal angles. In the case we get instead of (14):

$$T_1^1 = -T_2^2 = Q \quad T_2^1 = \sin \theta U, \quad T_1^2 = U / \sin \theta,$$

and again we have

$$I^2 = 0.5 T_i^k T_k^i = Q^2 + U^2.$$

Stokes parameters Q and U are linked with the potentials E and B as follows:

$$Q = D_1 E - D_2 B, \quad U = D_2 E + D_1 B, \quad (22)$$

and operators D_1 and D_2 are:

$$D_1 = \frac{1}{2} \left(\frac{\partial^2}{\partial \theta^2} - \cot \theta \frac{\partial}{\partial \theta} - \frac{1}{\sin^2 \theta} \frac{\partial^2}{\partial \varphi^2} \right) = \frac{1}{2} \left((1-x^2) \frac{\partial^2}{\partial x^2} - \frac{1}{1-x^2} \frac{\partial^2}{\partial \varphi^2} \right) \quad (23)$$

$$D_2 = \left(\frac{1}{\sin \theta} \frac{\partial^2}{\partial \theta \partial \varphi} - \frac{\cot \theta}{\sin \theta} \frac{\partial}{\partial \varphi} \right) = - \left(\frac{\partial^2}{\partial x \partial \varphi} + \frac{x}{1-x^2} \frac{\partial}{\partial \varphi} \right).$$

where $x = \cos \theta$. These operators are identical with expressions (2.22) and (2.23) in Ref. 27.

6.1.3. Spherical harmonics

Following to Refs. 14, reficiteglespa we use the representation of scalar (“electrical”), E , and pseudoscalar (“magnetic”), B , polarization potentials identical to (1):

$$E = \frac{1}{\sqrt{2\pi}} \sum_{\ell=2}^{\ell_{max}} \left(e_{\ell 0} f_{\ell}^0(x) + 2 \sum_{m=1}^{\ell} f_{\ell}^m(x) [e_{\ell m}^c \cos(m\varphi) - e_{\ell m}^s \sin(m\varphi)] \right), \quad (25)$$

$$B = \frac{1}{\sqrt{2\pi}} \sum_{\ell=2}^{\ell_{max}} \left(b_{\ell 0} f_{\ell}^0(x) + 2 \sum_{m=1}^{\ell} f_{\ell}^m(x) [b_{\ell m}^c \cos(m\varphi) - b_{\ell m}^s \sin(m\varphi)] \right), \quad (26)$$

$$f_{\ell}^m = \sqrt{(\ell+0.5) \frac{(\ell-m)!}{(\ell+m)!}} B_{\ell}^m, \quad 0 \leq m \leq \ell \leq \ell_{max}, \quad (27)$$

Here $B_{\ell}^m(x)$ and $f_{\ell}^m(x)$ are the associated Legendre functions (ordinary and normalized) and $e_{\ell m}$ and $b_{\ell m}$ are the coefficients of decomposition characterizing properties of polarization.

$$e_{\ell m}^c = \frac{1}{\sqrt{2\pi}} \int_{-1}^1 dx \int_0^{2\pi} d\varphi E(x, \varphi) f_{\ell}^m(x) \cos m\varphi, \quad (28)$$

$$e_{\ell m}^s = \frac{1}{\sqrt{2\pi}} \int_{-1}^1 dx \int_0^{2\pi} d\varphi E(x, \varphi) f_{\ell}^m(x) \sin m\varphi.$$

Similar expressions for the “magnetic” mode can be obtained by replacing of $e_{\ell m}^c$ & $e_{\ell m}^s$ with $b_{\ell m}^c$ & $b_{\ell m}^s$ and E with B .

As in the previous package the functions $f_{\ell}^m(x)$ are found recursively:

$$f_{\ell}^m(x) = x \sqrt{\frac{4\ell^2 - 1}{\ell^2 - m^2}} f_{\ell-1}^m - \sqrt{\frac{2\ell + 1}{2\ell - 3} \frac{(\ell-1)^2 - m^2}{\ell^2 - m^2}} f_{\ell-2}^m, \quad (30)$$

or

$$f_{\ell}^m = -\frac{2(m-1)}{\sqrt{\ell^2 - m^2 + \ell + m}} \frac{x f_{\ell}^{m-1}}{\sqrt{1-x^2}} - \sqrt{\frac{\ell+2-m}{\ell+1-m} \frac{\ell+m-1}{\ell+m}} f_{\ell}^{m-2}, \quad (31)$$

$$f_m^m = (-1)^m \sqrt{\frac{(2m+1)!!}{2(2m)!!}} (1-x^2)^{m/2}, \quad f_{m+1}^m = x\sqrt{2m+3}f_m^m. \quad (32)$$

Relation (30) starts with f_m^m and f_{m+1}^m (32) and generates functions f_ℓ^m for all $\ell \geq m$. Relation (31) starts with f_m^m and f_ℓ^0 and generates functions f_ℓ^m for all $1 \leq m \leq \ell$. In the case function f_ℓ^0 must be found with relation (30).

It is easy to see that

$$D_1 E = F_\ell^m [e_{\ell m}^c \cos(m\varphi) - e_{\ell m}^s \sin(m\varphi)], \quad (33)$$

$$D_2 E = \Phi_\ell^m [e_{\ell m}^c \sin(m\varphi) + e_{\ell m}^s \cos(m\varphi)], \quad (34)$$

where functions F_ℓ^m and Φ_ℓ^m are expressed through the normalized Legendre functions (30,31):

$$M_\ell F_\ell^m = \sqrt{\frac{2\ell+1}{2\ell-1}} (\ell^2 - m^2) \frac{x f_{\ell-1}^m}{1-x^2} + \frac{(m^2 - \ell) f_\ell^m}{1-x^2} - \frac{\ell(\ell-1)}{2} f_\ell^m, \quad (35)$$

$$M_\ell \Phi_\ell^m = \frac{m}{1-x^2} \left[\sqrt{\frac{2\ell+1}{2\ell-1}} (\ell^2 - m^2) f_{\ell-1}^m - (\ell-1) x f_\ell^m \right], \quad (36)$$

or by other way

$$M_\ell F_\ell^m = \frac{m-1}{1-x^2} m f_\ell^m - \frac{\ell^2 + \ell - 2m}{2} f_\ell^m - \sqrt{\frac{\ell^2 - m^2 + \ell - m}{1-x^2}} x f_\ell^{m+1}, \quad (37)$$

$$M_\ell \Phi_\ell^m = -m \left[\frac{\sqrt{(\ell+m+1)(\ell-m)}}{\sqrt{1-x^2}} f_\ell^{m+1} + (m-1) \frac{x}{1-x^2} f_\ell^m \right]. \quad (38)$$

Here

$$M_\ell^2 = 0.25(\ell+2)(\ell+1)\ell(\ell-1), \quad (39)$$

and functions F_ℓ^m and Φ_ℓ^m are normalized by condition

$$\int_{-1}^1 (F_\ell^m + \Phi_\ell^m)^2 dx = \int_{-1}^1 [(F_\ell^m)^2 + (\Phi_\ell^m)^2] dx = 1.$$

In particular,

$$F_m^m = \frac{m-1}{2M_m} m \frac{1+x^2}{1-x^2} f_m^m, \quad F_{m+1}^m = m x f_m^m \frac{\sqrt{2m+3}}{M_{m+1}} \left[\frac{m-1}{1-x^2} - \frac{m+1}{2} \right],$$

$$\Phi_m^m = -\frac{m(m-1)}{M_m(1-x^2)} x f_m^m, \quad \Phi_{m+1}^m = m f_m^m \frac{\sqrt{2m+3}}{M_{m+1}} \frac{1-mx^2}{1-x^2}, \quad (42)$$

Combining (22), (23), (25) and (26), we get for functions Q , & U :

$$Q_c^m(x) = \frac{1}{\sqrt{2\pi}} \int_0^{2\pi} d\varphi Q \cos m\varphi = \sum_{\ell=2}^{\ell_{max}} (F_\ell^m(x) e_{\ell m}^c - \Phi_\ell^m(x) b_{\ell m}^s), \quad (43)$$

$$Q_s^m(x) = \frac{1}{\sqrt{2\pi}} \int_0^{2\pi} d\varphi Q \sin m\varphi = \sum_{\ell=2}^{\ell_{max}} (-F_\ell^m(x)e_{\ell m}^s - \Phi_\ell^m(x)b_{\ell m}^c), \quad (44)$$

$$U_c^m(x) = \frac{1}{\sqrt{2\pi}} \int_0^{2\pi} d\varphi U \cos m\varphi = \sum_{\ell=2}^{\ell_{max}} (\Phi_\ell^m(x)e_{\ell m}^s + F_\ell^m(x)b_{\ell m}^c), \quad (45)$$

$$U_s^m(x) = \frac{1}{\sqrt{2\pi}} \int_0^{2\pi} d\varphi U \sin m\varphi = \sum_{\ell=2}^{\ell_{max}} (\Phi_\ell^m(x)e_{\ell m}^c - F_\ell^m(x)b_{\ell m}^s), \quad (46)$$

6.1.4. Spin-weight functions

Functions F_ℓ^m and Φ_ℓ^m do not form an orthogonal basis and to perform the further decomposition of polarization we need to use the normalized spin - weight spherical functions which can be defined as follows:

$$\lambda_{\ell,m}^+ = F_\ell^m + \Phi_\ell^m, \quad \lambda_{\ell,m}^- = F_\ell^m - \Phi_\ell^m, \quad (47)$$

$$\lambda_{\ell,m}^+(x) = (-1)^{m+\ell} \lambda_{\ell,m}^-(-x), \quad \lambda_{\ell,m}^-(-x) = (-1)^{m+\ell} \lambda_{\ell,m}^+(x), \quad (48)$$

These functions satisfy the self-adjoint equation:

$$\frac{d}{dx} \left[(1-x^2) \frac{d}{dx} \lambda_{\ell,m} \right] - \frac{4+m^2+4mx}{1-x^2} \lambda_{\ell,m} + \ell(\ell+1) \lambda_{\ell,m} = 0,$$

and, so, they are orthogonal for a given m (see, e.g., 30, 31 and references there). Some of this functions can be written directly:

$$\lambda_{m,m}^+ = A_{m,m} (-1)^m (1-x)^2 (1-x^2)^{\frac{m-2}{2}} = F_m^m + \Phi_m^m,$$

$$\lambda_{m+1,m}^+ = A_{m+1,m} (-1)^m (1-x)^2 (1-x^2)^{\frac{m-2}{2}} [2 + (m+1)x] = F_{m+1}^m + \Phi_{m+1}^m,$$

$$A_{m,m}^2 = \frac{m(m-1)(2m+1)!!}{(m+2)(2m+2)!!}, \quad A_{m+1,m}^2 = \frac{2m+3}{(m+3)(m-1)} A_{m,m}^2.$$

and using these relations functions $\lambda_{\ell,m}$ with $\ell > m+1$ can be evaluated recursively:

$$\lambda_{\ell,m} = \left(x + \frac{2m}{\ell(\ell-1)} \right) C_{\ell,m} \lambda_{\ell-1,m} - \frac{C_{\ell,m}}{C_{\ell-1,m}} \lambda_{\ell-2,m}, \quad (53)$$

$$C_{\ell,m} = \sqrt{\frac{\ell^2(4\ell^2-1)}{(\ell^2-m^2)(\ell^2-4)}}.$$

$$\int_{-1}^1 dx [F_\ell^m(x)F_k^m(x) + \Phi_\ell^m(x)\Phi_k^m(x)] = \delta_{k\ell},$$

$$\int_{-1}^1 dx [F_\ell^m(x)\Phi_k^m(x) + \Phi_\ell^m(x)F_k^m(x)] = 0.$$

This means that coefficients for the decomposition of Q and U can be found from (43-46) as follows:

$$e_{\ell m}^c = \int_{-1}^1 dx [\Phi_{\ell}^m(x) U_s^m(x) + F_{\ell}^m(x) Q_c^m(x)], \quad (57)$$

$$e_{\ell m}^s = \int_{-1}^1 dx [\Phi_{\ell}^m(x) U_c^m(x) - F_{\ell}^m(x) Q_s^m(x)], \quad (58)$$

$$b_{\ell m}^c = \int_{-1}^1 dx [F_{\ell}^m(x) U_c^m(x) - \Phi_{\ell}^m(x) Q_s^m(x)], \quad (59)$$

$$b_{\ell m}^s = \int_{-1}^1 dx [-F_{\ell}^m(x) U_s^m(x) - \Phi_{\ell}^m(x) Q_c^m(x)], \quad (60)$$

For numerical analysis of the polarization maps together with the temperature fluctuations it is convenient to use relations (27 - 38) and (57 - 60) instead of the recursive relations (53). Inverse problem that is the construction of the polarization maps from coefficients $e_{\ell m}$ & $b_{\ell m}$ can also be solved using relations (43-46).

6.1.5. Spectra of the anisotropy and polarization

Four power spectra can be introduced for the temperature, electrical and magnetic Stokes parameters, they are:

$$C_{\ell}^T = \frac{1}{2\ell + 1} \sum_{m=-\ell}^{\ell} |a_{\ell m}|^2,$$

$$C_{\ell}^E = \frac{1}{2\ell + 1} \sum_{m=0}^{\ell} [(e_{\ell m}^c)^2 + (e_{\ell m}^s)^2], \quad (62)$$

$$C_{\ell}^B = \frac{1}{2\ell + 1} \sum_{m=0}^{\ell} [(b_{\ell m}^c)^2 + (b_{\ell m}^s)^2],$$

$$C_{\ell}^{TE} = \frac{1}{2\ell + 1} \sum_{m=0}^{\ell} [a_{\ell m}^c e_{\ell m}^c + a_{\ell m}^s e_{\ell m}^s],$$

When averaged over the sky, the mean square temperature anisotropy is

$$\langle \Delta T^2 \rangle = T_0^2 \sum_{\ell=2}^{\infty} \frac{2\ell + 1}{4\pi} C_{\ell}^T, \quad (65)$$

where T_0 is the temperature of the CMB. The mean square of polarization is

$$\langle I^2 \rangle = \frac{1}{2} \langle Q^2 + U^2 \rangle = \frac{1}{2} [\langle E_*^2 \rangle + \langle B_*^2 \rangle]$$

where

$$\langle E_*^2 \rangle = T_0^2 \sum_{\ell=2}^{\infty} \frac{2\ell+1}{4\pi} C_\ell^E, \quad (67)$$

$$\langle B_*^2 \rangle = T_0^2 \sum_{\ell=2}^{\infty} \frac{2\ell+1}{4\pi} C_\ell^B, \quad (68)$$

More details can be found in, for example, Refs. 32, 33, 34, 27.

6.2. Incorporating of the polarization to the GLESP code

To realize algorithms described above, special procedures had been created. We had developed this code in parallel in the two algorithmic languages, GNU C and FORTRAN-77. The procedures have been designed both like subroutines and package utilities implementing in the GLESP pixelization scheme.

Two commands of GLESP-pol should be used for calculation of polarization, namely, ‘*polmap*’ and ‘*polalm*’. ‘*polmap*’ calculates Q and U-polarization maps by coefficients of E- and B- polarization modes. ‘*Polalm*’ calculates coefficients of E- and B-polarization modes by Q- and U-polarization maps, respectively. E- and B-coefficients recorded as $a_{\ell m}$ -format files, and Q- and U-maps recorded like GLESP maps. Both procedures can be used for temperature-spherical harmonics transformations too. These procedures are included to the GLESP package, version 2.0. The programs use the fast Fourier transform FFTW-3.2.1 Ref. 35.

The program ‘*difmap*’ is developed for standard polarization transforms to calculate a polarization angle $PA = 1/2 \arctan(U/Q)$ and an intensity $I = \sqrt{Q^2 + U^2}$. Both values can be plotted with the GLESP drawing procedure ‘*f2fig*’.

6.3. Accuracy restrictions

Both temperature and polarization maps and spectra processed by the GLESP package are determined in main by four parameters. First of all, it is the maximal number of harmonics under consideration, ℓ_{max} (25). The second one is the number of rings used for map presentation, N_θ . By definition, we must have $N_\theta \geq 2\ell_{max}$. The third one is the number of pixels for each ring of the map, $N_\phi^i(\theta_i)$. If we like to use the same angular resolution in azimuthal and polar directions than, evidently, we must take $N_\phi(\pi/2) \approx 2N_\theta$, and $N_\phi^i(\theta_i)$ decreases progressively away from the equator. The fourth one is the Nyquist parameter, N_y , which regulates the precisions achieved by calculations.

The precision depends upon the choice $N_\theta \geq 2\ell_{max}$ and the Nyquist parameter, N_y . Thus, the orthogonality of spherical harmonics Y_ℓ^m on the sphere is achieved only if number of pixels for each ring is at least two times larger than number of harmonics we use in our analysis, $N_\phi^i(\theta_i) \geq 2m$, $0 \leq m \leq \ell$ (Nyquist restriction, $N_\phi^i(\theta_i) \geq m/N_y \geq 2m$, $N_y \leq 0.5$). Since we try to keep the same pixel area for

different latitude, this condition is *not completely satisfied* anymore because rings with number of pixels $N_\phi^i(\theta_i) \leq 2m$ drop out from any calculations.

Fortunately, the influence of these restrictions on the precision achieved is moderate because the contribution of polar areas is quite small for almost all harmonics by the following reason:

- Spin-weighted harmonics satisfy ${}_{\pm 2}Y_{\ell m} \sim \sin^{m-2}(\theta)$ for $m > 2$. This means that harmonics with high m are weighted negligible everywhere apart from the equator, where number of pixels is enough for orthogonality.
- Harmonics with small $m \leq m_{min} = N_y \times N_{min}$ are orthogonal.
- Therefore, it can be expected that the harmonics with $m \sim m_{min}$ are the most dangerous. For such harmonics rings nearby the poles have number of pixels smaller than $2 \times m$ and these parts of the sphere spoil the picture. However, the weight of these parts of the sphere is proportional to $\sin^{m-2}(\theta)$ and tends to be zero for $\theta \rightarrow 0, \pi$.

To accelerate the computations we remain in the calculations only larger terms restricted by conditions $|f_\ell^m(x)| \geq \varepsilon$, $|F_\ell^m|, |\Phi_\ell^m| \geq \varepsilon$ where ε depends upon ℓ and required precision and, so, is determined in practice. Our tests show that the choice $\varepsilon = \varepsilon_1$ for $\ell \leq 500$ and $\varepsilon = \varepsilon_2$ for $\ell \geq 500$ allows to moderately decrease the calculation time and weakly change the precision achieved.

We can conclude, that for a given ℓ_{max} the reasonable precision can be achieved for the parameters :

$$N_\theta = (2.5 - 3)\ell_{max}, \quad N_\phi = 2 \times N_\theta, \quad N_{min} = 9 - 11, \quad N_y = 0.5, \quad (69)$$

and

$$\varepsilon_1 \approx 10^{-10}, \quad \varepsilon_2 \approx 10^{-4}.$$

Evidently, the precision achieved increases for larger N_θ and N_ϕ , however, is accompanied by corresponding fast growth of the calculation time. Perhaps, for calculations of polarization the better results can be achieved with the repixelisation of the map in accordance with the net of roots of the spin - weight functions $\lambda_{\ell,m}^\pm$ (47) instead of the Legendre polynomials (5) and corresponding choice of the weighting coefficients (6).

6.4. Data format

Developing the GLESP package for polarization calculation, we should change a format of data representation. We introduce two types of the format describing $a_{\ell m}$ -coefficients and maps.

In the first case, we can use the standard $a_{\ell m}$ - coefficients data, which contain index describing number of ℓ and m modes corresponding to the HEALPix, real and imaginary parts of $a_{\ell m}$. These three parameters are described by three-fields records of the FITS Binary Table Ref. 36. Map data are described by the three- fields Binary

Table FITS format containing a vector of $x_i = \cos \theta$ positions, a vector of numbers of pixels per each layer N_{ϕ_i} , and set of temperature values in each pixel recorded by layers from the North Pole. All these data description formats are used separately for each type and polarization mode data, i.e. maps for temperature anisotropy, Q and U-data are contained in singles files, and $a_{\ell m}$ and E and B-modes coefficients are stored in singles file too.

The second type of the data representation format is similar to HEALPix one. In this case, data are unified in 3 extensions containing maps with anisotropy, Q- and U-polarization data or $a_{\ell m}$ -coefficients of temperature expansions and E- and B-mode, respectively. Files with coefficients in GLESP and in HEALPix have the same format. Each of three FITS extensions of GLESP files with maps contains three fields described above.

So, using two formats of data representation a user can easily select a path of one's data processing including or excluding any type of polarization or anisotropy data.

